International Journal of Engineering Research & Technology (IJERT)
ISSN: 2278-0181
Vol. 14 Issue 08, August - 2025

Design and Performance Analysis of Deformed Wheels for Dual-Mode Wheels on Complex Pavement

Xinyu Jia (Corresponding Author)
School of Mechanical Engineering
Tianjin University of Technology and Education
Tianjin 300222, China

Shijie Guo
School of Mechanical Engineering
Tianjin University of Technology and Education
Tianjin 300222, China

***Abstract*—To address the challenges of inefficient mode switching and inadequate dynamic stability in wheel-legged robots operating on complex terrains, this study proposes a novel dual-mode deformable wheel mechanism. The design employs a crank-rocker-guide rod tandem transmission system integrated with a self-locking structure, enabling rapid and reliable transitions between wheeled and legged operational modes. Through mechanical modeling, the forward and reverse obstacle-crossing characteristics of the wheel-leg mechanism are analyzed, and the optimal number of wheel-legs is determined. Furthermore, a quantitative relationship between the maximum obstacle-crossing height and the wheel diameter is derived. Kinematic models for both synchronized gait and diagonal gait are established to investigate the variations in displacement, velocity, and acceleration under these two gait patterns. The results demonstrate that the proposed deformable wheel mechanism exhibits significant enhancements in obstacle-crossing capability and motion stability compared to conventional designs, offering a promising technical solution for the development of mobile robots in complex terrain environments.**

***Keywords*— Deformed hub; wheel - leg robot; obstacle performance; gait planning; kinematics analysis**

I. INTRODUCTION

Industrial mobile robots exhibit excellent environmental adaptability and operational reliability. They are progressively replacing manual labor in performing high-risk, high-intensity, and repetitive tasks (1). With the rapidly growing demand for operation in unstructured environments, mobile robot technology has ushered in new developmental opportunities (2). As a crucial branch within the field of intelligent robotics, mobile robots integrate core functionalities including environmental perception, dynamic decision-making, motion planning, and behavior control (3)(4)(5). They have demonstrated significant application value in domains such as disaster relief (6), military reconnaissance (7), space exploration (8), pipeline inspection (9), and livelihood services (10).

In terms of adaptability to complex terrain, wheel-legged robots possess unique structural advantages. They combine the efficient mobility of wheeled mechanisms with the flexibility of legged mechanisms (11)(12)(13), making them a key research direction in mobile robotics. In recent years, scholars both domestically and internationally have achieved significant breakthroughs in bionic locomotion mechanisms (14), intelligent control systems (15), and novel actuation methods (16). Comparatively, traditional wheeled mobile mechanisms offer distinct advantages in terms of high movement speed and control simplicity (17). However, they exhibit significant limitations in unstructured environments (18). Research and exploration into novel mobile mechanism design are therefore of great importance for enhancing the motion efficiency and terrain adaptability of balancing robots (19).

Currently, wheel-legged robots still face numerous challenges in balancing complex terrain adaptability with motion efficiency. A planetary wheel-leg architecture demonstrated by Zhang et al. employs an epicyclic gear train that allows a 100-mm-diameter wheel to climb vertical steps up to twice its own radius; nevertheless, the additional gear stages and locking mechanisms increase part count by 38% compared with a conventional rigid wheel, making compact integration difficult (20). To reduce mechanical intricacy, Kim et al. proposed a six-spoke deformable rim that folds via pin joints located at 60° intervals. Field trials on simulated lunar regolith showed reliable negotiation of 15-cm-high rocks, yet the folding sequence relies on high-resolution pressure sensors whose calibration drifts >5% after repeated thermal cycling between −150°C and +100°C, limiting long-term reliability (21). Drawing inspiration from cockroach locomotion, Case Western Reserve University’s Mini-WHEGS v3 combines alternating spoke wheels with passive, compliant tarsi to achieve a running speed of 1.2 m/s while clearing obstacles 1.5 times the wheel diameter. The design, however, requires precision-machined aluminium flexures and miniature ball bearings that raise the Bill-of-Materials cost by a factor of four relative to standard rover wheels (22). The aforementioned studies indicate that existing wheel-legged mechanisms still encounter bottlenecks such as low mode-switching efficiency (23), insufficient parameter adaptability (24), and poor dynamic stability (25).

To address these limitations, this study proposes a dual-mode deformable hub design enabling dynamic switching between wheeled and legged configurations. A series transmission scheme combining crank-rocker and guide rod mechanisms is introduced. This scheme, integrated with a self-locking mechanism, facilitates rapid mode switching. This approach aims to enhance the motion efficiency and environmental adaptability of wheel-legged robots, offering a novel concept for the design of high-dynamic mobile mechanisms.

II. STRUCTURAL AND MECHANICAL ANALYSIS OF DUAL-MODE DEFORMABLE HUB

A. design of the dual-mode deformable hub scheme

In order to ensure the applicability of the dual-mode deformable hub in mobile robots, the operational requirements for obstacle crossing and traversal on flat terrain were analyzed. A dual-mode deformable hub structure was designed to enable free switching between these two operational modes, thereby accommodating both high-speed movement and enhanced stability requirements. Through an analysis of the performance characteristics of various wheel-leg configurations, the specific wheel-leg mechanism investigated in this study was selected. A series of analyses and investigations were subsequently conducted on this mechanism.

a) Non-Circular Design Based on the Slider-Crank Mechanism

This scheme utilizes the slider-crank mechanism as the foundational principle to achieve the transformation between the wheeled and legged configurations, fulfilling the deformation objective. The stability of the transmission is enhanced by incorporating a parallel linkage combining a double-rocker mechanism and the slider-crank mechanism. A conceptual diagram of the scheme is shown in figure 1.

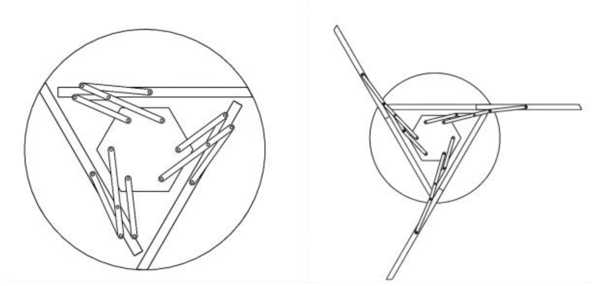

Fig. 1. Slider-crank series double-rocker mechanism

b) Quasi-Circular Design Based on Crank-Rocker-Guide Rod Mechanism

Motion is transmitted from the motor’s rotating shaft to the hook-shaped claw through a series-connected crank-rocker and crank-guide-rod mechanism. This configuration provides high hub-space-utilization efficiency and enhanced structural stability. The conceptual design is illustrated in figure 2.

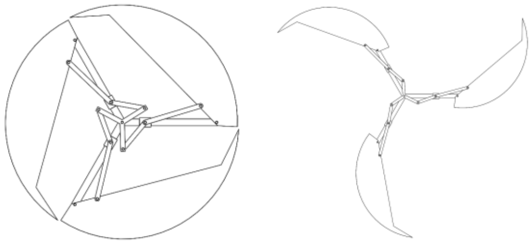

Fig. 2. Quasi-circular design scheme based on crank-rocker-guide rod mechanism

As shown in figure 3, while the non-circular design offers deformation convenience, the quasi-circular scheme enables dual-directional obstacle-crossing strategies. Crucially, this design demonstrates superiority in maximum obstacle-crossing height and, owing to its engineered arcuate profile, delivers more stable performance when traversing complex irregular obstacles. Consequently, the quasi-circular crank-rocker-guide rod mechanism was selected as the dual-mode deformable hub for this study, with detailed analyses performed accordingly.

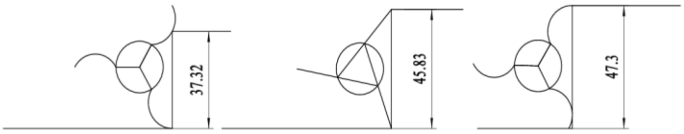

Fig. 3. Wheel-leg scheme obstacle-crossing height comparison

B. Wheel-Leg Parameters and Force Analysis

As the arc-shaped wheel-leg arm exhibits distinct cross-sectional profiles on its anterior and posterior sides, their obstacle-crossing capabilities differ significantly. Defining counterclockwise rotation as forward mode and clockwise rotation as reverse mode, kinematic analysis reveals:

Forward rotation: The arc-profile end initiates ground contact, enabling smooth traversal of low-height obstacles.

Reverse rotation: The linear-profile end contacts ground first. While this compromises stability, it achieves superior obstacle-crossing height, allowing terrain-adaptive gait planning.

For maximum obstacle-height analysis, the reverse mode configuration is adopted (Figure 3). The obstacle height H_S satisfies:

$$H_S = R\left(\sin\frac{\varphi_s}{2} + \cos\theta_s\right) \tag{1}$$

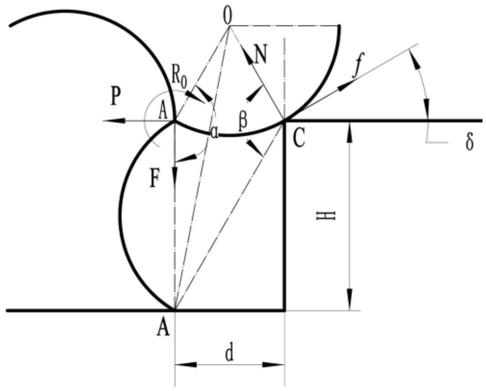

Fig. 4. Stress analysis diagram of single spoke

In the expression, H_S denotes the obstacle-crossing height corresponding to s wheel-legs, R represents the maximum radius of the wheel-leg, φ_s signifies the included angle between adjacent wheel-leg spokes, and θ_s indicates the angle between the wheel-leg-ground contact point and the vertical plane. Through analytical derivation, the following expression is obtained:

$$\begin{aligned} H_3 &= 1.732R; \\ H_4 &= 1.414R; \\ H_6 &= 1.5R; \\ H_8 &= 1.38R; \\ H_{10} &= 1.31R \end{aligned} \tag{2}$$

Therefore, the maximum height of obstacle crossing decreases with the increase of s when rotating in the reverse direction.

When analyzing the maximum forward obstacle-surmounting height, the maximum obstacle-surmounting height is limited by the friction force due to the contact between the arc surface and the step surface. It is necessary to analyze the force of single-wheel leg obstacle crossing.

As shown in figure 4, F and P are the vertical and horizontal portions of the robot body on the wheel legs, respectively, N and f are the bearing capacity and friction force of the step on the wheel leg, H is the height of the step, R0 is the torque of the robot acting on the mechanism, P is the angle of the friction provided by the step for the mechanism to the obstacle. The following equilibrium equation is given:

$$\begin{cases} P - f\cos\delta + N\sin\delta = 0 \\ F - f\sin\delta - N\cos\delta = 0 \\ R_0 - M_N - M_f = 0 \end{cases} \tag{3}$$

At this time, if point A is in the unstressed state and point C is in the critical sliding state, then the friction force at point C can be expressed as:

$$f = \mu N \tag{4}$$

Where μ is the coefficient of static friction between the wheel leg and the stair surface, and the equilibrium equation of point C in the horizontal direction can be written as:

$$P = N\left(\mu\cos\delta - \sin\delta\right) \tag{5}$$

It can be further simplified as:

$$\frac{P}{N} = \left(\mu\cos\delta - \sin\delta\right) \tag{6}$$

Among them, when μ is arbitrary and $\frac{P}{N} > 0$, the friction horizontal component force of the mechanism is used as the driving force to resist the horizontal component force from the body and the horizontal component force of the support force, and the obstacle crossing is completed. When $\frac{P}{N} < 0$, the horizontal component of the body is used as the driving force, and the body is crossing the obstacle. Take $\mu = 0.4d$, calculate the corresponding $\frac{P}{N}$ value when $\delta = 0°、20°、40°、60°、80°$, and then calculate the critical angle of obstacle crossing. Draw the result as a curve as shown in figure 5:

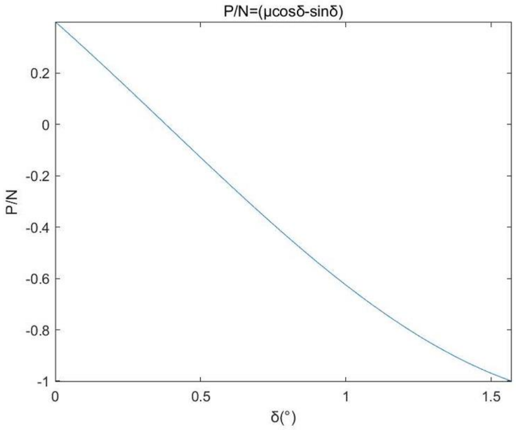

Fig. 5. Functional diagram of mode-switching limit angles for wheel-leg mechanism

And when $\frac{P}{N}=0$, δ is about 21.804°. This angle is called the limit angle of the variable hub mechanism when the obstacle crossing and moving state are switched. When $\delta < 21.804^{\circ}$, the mechanism is in a moving state at this time, otherwise the mechanism is avoiding obstacles.

Based on the above analysis, the obstacle-crossing process of the wheel-legged robot is simulated by analyzing the sequential posture variations of front and rear legs during different traversal stages (figure 6). The complete process can be classified into four characteristic phases according to the dynamic interaction relationships between the front/rear wheel-leg assemblies and the obstacle.

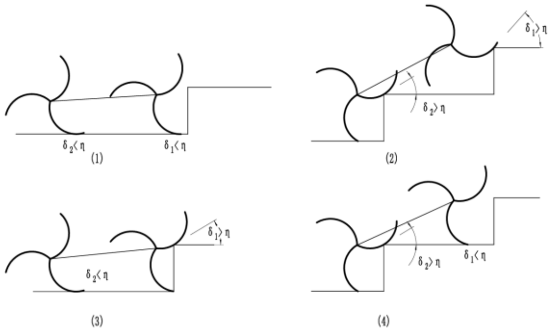

Fig. 6. Analysis of obstacle crossing of front and rear wheel legs

Taking (3) as an example, further stress analysis is carried out. The overall force analysis is carried out as shown in figure 7:

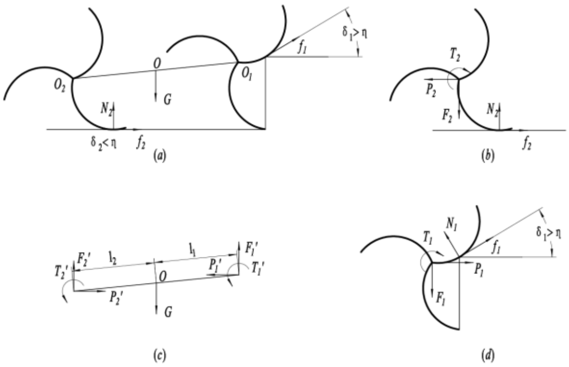

Fig. 7. Force analysis diagram of front wheel obstacle negotiation

Among them, f_1、N_1 and f_2、N_2 are the friction and pressure when the front and rear wheels of the robot contact with the pedal. The vertical and vertical components used by the P_1、F_1 and P_2、F_2 robots on the front and rear wheels respectively ; $P_1^{'}$、$F_1^{'}$ 、 and $P_2^{'}$、$F_2^{'}$ are the reaction force of the front and rear wheel legs to the hub center respectively; T_1 and T_2 are the torque applied by the hub to the front and rear wheel legs, respectively. $T_1^{'}$ and $T_2^{'}$ are the reaction torque of the front and rear wheel legs to the hub center. G is the gravity of the whole mechanism.

The force analysis of the robot shows that:

$$\begin{cases} f_1\cos\delta_1 - N_1\sin\delta_1 + f_2\cos\delta_2 - N_2\sin\delta_2 = 0 \\ G - f_1\sin\delta_1 - N_1\cos\delta_1 - f_2\sin\delta_2 - N_2\cos\delta_2 = 0 \\ M_{ON2} - M_{Of2} - M_{ON1} - M_{Of1} = 0 \end{cases} \tag{7}$$

Where M_{ON_1}、M_{ON_2} is the torque of N_1、N_2 to point O;

M_{Of_1}、M_{Of_2} is the torque of f_1、f_2 to O point.

From the force balance analysis of the robot, it can be obtained:

$$\begin{cases} P_1^{'} - P_2^{'} = 0 \\ G - F_1^{'} - F_2^{'} = 0 \\ T_1^{'} + T_2^{'} + M_{OP1}^{'} + M_{OP2}^{'} + M_{OF1}^{'} - M_{OF2}^{'} = 0 \end{cases} \tag{8}$$

Where M'_{OP_1}、M'_{OP_2} is the torque of P'_1、P'_2 to point O;

M'_{OF1}、M'_{OF2} is the torque of F'_1、F'_2 to point O.

It can be concluded from the analysis of the force balance of the front wheel:

$$\begin{cases} P_1 + f_1\cos\delta_1 - N_1\sin\delta_1 = 0 \\ F_1 - f_1\sin\delta_1 - N_1\cos\delta_1 = 0 \\ T_1 - M_{O1N1} - M_{O1f1} = 0 \end{cases} \tag{9}$$

It is obtained by the force balance of the rear wheel leg of the robot:

$$\begin{cases} P_2 - f_2\cos\delta_2 + N_2\sin\delta_2 = 0 \\ F_2 - f_2\sin\delta_2 - N_2\cos\delta_2 = 0 \\ T_2 - M_{O2N2} - M_{O2f2} = 0 \end{cases} \tag{10}$$

The torque applied to the robot is:

$$\begin{cases} M_{OP1'} = P_1'l_1\sin\gamma \\ M_{OP2'} = P_2'l_2\sin\gamma \\ M_{OF1'} = F_1'l_1\cos\gamma \\ M_{OF2'} = F_2'l_2\cos\gamma \end{cases} \tag{11}$$

When $\delta_2 = 0$, the maximum driving force provided by the rear wheel (driving wheel) to the body is

$$P_{2\max} = \frac{\mu}{(l_1 + l_2)(1 - \mu\tan\gamma)}\left(Gl_1 + \frac{T_1 + T_2}{\cos\gamma}\right) \tag{12}$$

The maximum values of δ_1 is:

$$\delta_{1\max} = \arctan\left(\frac{\mu^2 G}{\mu G - (1 + \mu^2)P_{2\max}}\right) \tag{13}$$

It can be seen from the above formula that when the rear wheel is the driving wheel and $\delta_2 = 0$, if the mechanism satisfies $\delta_1 < \delta_{1\max}$, the wheel leg in contact with the front wheel can cross the step.

Similarly, when the current wheel is the driving wheel and $\delta_1 = 0$, the maximum driving force $P_{1\max}$ of the front wheel is:

$$P_{1\max} = \frac{\mu}{(l_1 + l_2)(1 - \mu\tan\gamma)}\left(Gl_2 + \frac{T_1 + T_2}{\cos\gamma}\right) \tag{14}$$

The maximum value of $\delta_{2\max}$ is:

$$\delta_{2\max} = \arctan\left(\frac{\mu^2 G}{\mu G - (1 + \mu^2)P_{1\max}}\right) \tag{15}$$

In summary, under the condition of known parameters such as friction coefficient, stair size, robot weight and centroid position, the overturn condition of the mechanism under single wheel contact obstacle can be calculated.

Therefore, as long as the angle between the tangent of the contact point of the wheel leg and the step and the step is less than 54.26°, the wheel leg may cross the obstacle, so the obstacle height with the maximum forward rotation of different wheel legs can be determined, as shown in figure 8:

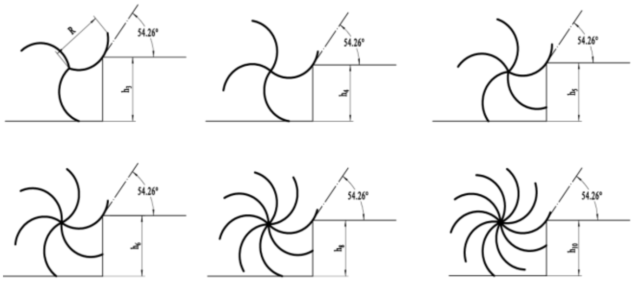

Fig. 8. Comparison of maximum obstacle-crossing height under different number of wheel legs

Under the forward and reverse rotation of the analysis mechanism, the obstacle height values under the number of wheel legs are extracted and compared, and the broken line diagram shown in figure 9 is obtained. In the case of forward and reverse rotation, the function trend is basically the same. In order to ensure that the mechanism has good obstacle crossing function in the dual mode, the number of wheel legs $s = 3$ is selected as the final number of wheel legs of the deformation mechanism.

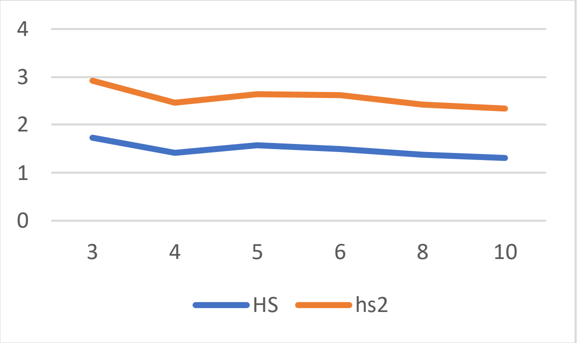

Fig. 9. Wheel-leg configuration vs. obstacle negotiation performance diagram

III. 3 DIAGONAL GAIT PLANNING AND SYNCHRONIZED GAIT PLANNING FOR DUAL-MODE DEFORMABLE HUB MECHANISM

A. Synchronized Gait Planning and Analysis for Dual-Mode Deformable Hub

The synchronized gait refers to the motion analysis when all four wheels maintain identical speed and phase synchronization, where all four wheel-legs remain in the stance phase at any given moment. The stance phase indicates the state where a robot's leg contacts the ground to provide support, and the average number of supporting legs during multi-legged walking can be represented by the stability coefficient δ_p , expressed as:

$$\delta_p = s\square\beta_p \tag{16}$$

In this context, β_p represents the duty cycle coefficient, defined as the ratio of a single wheel-leg's support time to the complete gait cycle duration. When the robot moves in synchronized gait mode, since all four wheel-legs remain in the stance phase simultaneously, the duty cycle coefficient $\beta_p = 1$ and the stability coefficient $\delta_p = 4$, indicating the robot achieves optimal stability under this configuration.

Let $O\text{-}XYZ$ denote the ground-fixed reference frame, while $O_i\text{-}X_iY_iZ_i$ $(i = 1, 2, 3, 4)$ represent the wheel-attached frames. The body frame is $O_o\text{-}X_oY_oZ_o$ defined at the robot's geometric center. The initial configuration aligns axis OZ with vector O_oZ_o under the rigid-body assumption. The robot's centroid position w in global coordinates can then be expressed by Equation (17):

$$w = \begin{bmatrix} X_{O_0} & Y_{O_0} & Z_{O_0} \end{bmatrix} \tag{17}$$

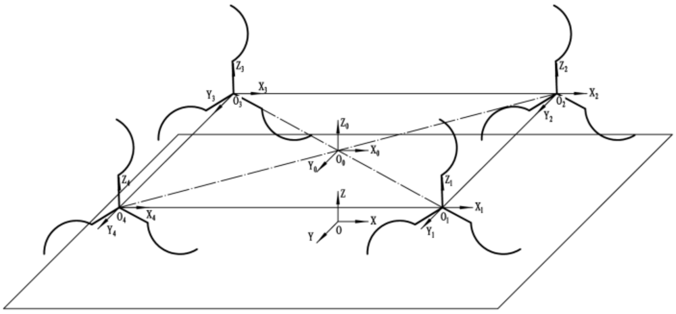

Fig. 10. Four-wheel coordinate system

According to the geometric relationship, the following conclusions can be drawn:

$$\begin{bmatrix} X_{O_i} & Y_{O_i} & Z_{O_i} \end{bmatrix} = \begin{bmatrix} X_{O_0} & Y_{O_0} & Z_{O_0} \end{bmatrix} + \begin{bmatrix} \Delta X_i & \square Y_i & \Delta Z_i \end{bmatrix} \tag{18}$$

Among them, X_{0_i}、Y_{0_i}、Z_{0_i} represents the position coordinates of the geometric center O_i of each wheel leg relative to the ground coordinate system ; the bias distance of ΔX_{0_i}、ΔY_{0_i}、ΔZ_{0_i} relative to O_0 in X, Y and Z directions has the following relationship:

$$\begin{cases} \Delta X_1 + \Delta X_3 = 0 \\ \Delta X_2 + \Delta X_4 = 0 \\ \Delta Y_1 + \Delta Y_3 = 0 \\ \Delta Y_2 + \Delta Y_4 = 0 \\ \Delta Z_1 + \Delta Z_3 = 0 \\ \Delta Z_2 + \Delta Z_4 = 0 \end{cases} \tag{19}$$

The combination of Equation (17), Equation (18) and Equation (19) can be obtained:

$$\begin{aligned} w &= \begin{bmatrix} X_{O_0} \backslash & ;Y_{O_0} & Z_{O_0} \end{bmatrix} \\ &= \frac{\begin{bmatrix} X_{O_1} \backslash & Y_{O_1} & Z_{O_1} \end{bmatrix} + \begin{bmatrix} X_{O_3} & Y_{O_3} & Z_{O_3} \end{bmatrix}}{2} \\ &= \frac{\begin{bmatrix} X_{O_2} & Y_{O_2} & Z_{O_2} \end{bmatrix} + \begin{bmatrix} X_{O_4} & Y_{O_4} & Z_{O_4} \end{bmatrix}}{2} \end{aligned} \tag{20}$$

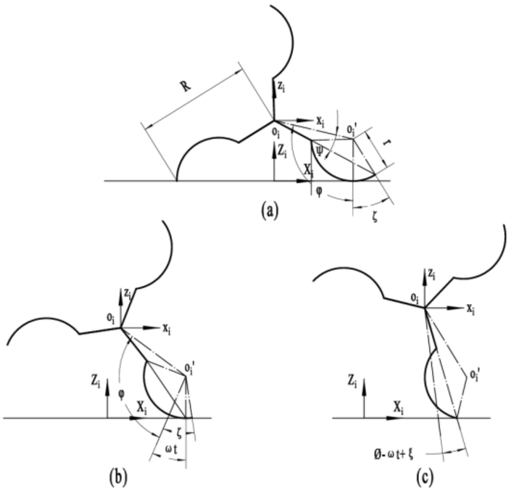

Fig. 11. Determination of geometric parameters of wheel legs

The kinematic behavior of the wheel-leg mechanism exhibits similarities to most legged systems, where critical parameters including the instantaneous rotation center height and velocity are not constant but demonstrate periodic variations corresponding to different motion phases. Taking the configuration presented in figure 11-a as the reference state, the motion cycle of this mechanism can be categorized into two sequential phases: during the initial phase (corresponding to figure 11-b), the curved rim maintains continuous dynamic contact with the ground surface while performing pure rolling motion, with the contact point progressively shifting along the wheel-leg profile; subsequently, in the secondary phase (as shown in figure 11-c), the motion transitions to fixed-point contact at the spoke tip, causing the mechanism to exhibit pendulum-like rotation about this stationary contact point. Through systematic geometric analysis, the time-dependent displacement functions $X_i(t)$ and $Z_i(t)$ of the wheel-leg's rotation center along both horizontal and vertical directions can be mathematically derived, thereby establishing the trajectory equation of the system's center of mass as follows:

$$X_{xi}=\begin{cases} p-r\sin\left[\left(\varphi+\omega(t-kT)\right)\right]\ldots \\ +\omega r(t-kT)+r\sin\beta\Rightarrow kT\le t\le kT+\dfrac{\xi}{\omega} \\ p+\xi r-R\sin\left[\psi-\omega(t-kT)+\xi\right]\ldots \\ +r\sin\varphi\Rightarrow kT+\dfrac{\xi}{\omega}\le t\le kT+\dfrac{2\pi}{3\omega} \end{cases} \quad (21)$$

$$X_T=X_i=(1+\sqrt{3})X_{xi} \quad (22)$$

$$Z_{xi}=\begin{cases} 2r\sin^2\left[\dfrac{\varphi+\omega(t-kT)}{2}\right] & kT\le t\le kT+\dfrac{\xi}{\omega} \\ R\cos\left[\psi-\omega\left(t-kT\right)+\xi\right] & kT+\dfrac{\xi}{\omega}\le t\le kT+\dfrac{2\pi}{3\omega} \end{cases} \quad (23)$$

$$Z_T=Z_i=(1+\sqrt{3})Z_{xi} \quad (24)$$

Among them, $\xi=0.328\pi$; $\varphi=0.571\pi$; $p=k\left[\xi r-R\sin(\psi-\dfrac{2\pi}{3}+\xi)+r\sin\varphi\right]$; The gait Cycle $T=2\pi/3\omega, k=0,1,2,3\ldots\ldots$

The above velocity equation is differentiated by time t, and the law of the velocity of the center of mass in the horizontal and vertical directions with time can be derived when the robot moves in a synchronous gait:

$$V_{Tx}=\begin{cases} -(1+\sqrt{3})\left\{\omega r\cos\left[\varphi+\omega(t-kT)\right]+\omega r\right\} \\ \Rightarrow kT\le t\le kT+\dfrac{\xi}{\omega} \\ (1+\sqrt{3})\left\{\omega R\cos\left[\psi-\omega\left(t-kT\right)\right]+\xi\right\} \\ \Rightarrow kT+\dfrac{\xi}{\omega}\le t\le kT+\dfrac{2\pi}{3\omega} \end{cases} \quad (25)$$

$$V_{Tz}=\begin{cases} \left(1+\sqrt{3}\right)\left\{\omega r\sin\left[\varphi+\omega(t-kT)\right]\right\} \\ \Rightarrow kT\le t\le kT+\dfrac{\xi}{\omega} \\ \left(1+\sqrt{3}\right)\left\{\omega R\sin\left[\psi-\omega(t-kT)+\xi\right]\right\} \\ \Rightarrow kT+\dfrac{\xi}{\omega}\le t\le kT+\dfrac{2\pi}{3\omega} \end{cases} \quad (26)$$

Similarly, the above velocity equation is differentiated by time t, and the law of acceleration of the center of mass in the horizontal and vertical directions with time is obtained:

$$a_{Tx}=\begin{cases}(1+\sqrt{3})\left\{\omega^2 r\sin[\varphi+\omega(t-kT)]\right\}\\ \Rightarrow kT\le t\le kT+\dfrac{\xi}{\omega}\\ (1+\sqrt{3})\left\{\omega^2 R\sin\left[\psi-\omega\left(t-kT\right)\right]+\xi\right\}\\ \Rightarrow kT+\dfrac{\xi}{\omega}\le t\le kT+\dfrac{2\pi}{3\omega}\end{cases}\tag{27}$$

$$a_{Tz}=\begin{cases}\left(1+\sqrt{3}\right)\left\{\omega^2 r\cos[\varphi+\omega(t-kT)]\right\}\\ \Rightarrow kT\le t\le kT+\dfrac{\xi}{\omega}\\ \left(1+\sqrt{3}\right)\left\{\omega^2 R\cos[\psi-\omega(t-kT)+\xi]\right\}\\ \Rightarrow kT+\dfrac{\xi}{\omega}\le t\le kT+\dfrac{2\pi}{3\omega}\end{cases}\tag{28}$$

B. Diagonal Gait Planning and Analysis for Dual-Mode Deformable Hub

The characteristics of the cross-symmetric gait are as follows: In the motion timing configuration, the two groups of wheels and legs in the diagonal line maintain complete synchronization, while there is a $\frac{\pi}{3}$ phase lag between the adjacent two groups of wheels and legs, and each wheel and leg maintains an equal angular velocity drive. When the supporting wheel leg in the supporting state enters the moment of transition from the ground, the opposite wheel leg, which was originally in the suspended state, synchronously establishes the ground contact, forming a persistent alternating mechanism of double limb support and double limb swing. The action cycle ratio parameter $\beta_p=0.5$, the motion stability parameter

$\delta_p=2$.

From the time dimension analysis, the support period and swing dynamics of the gait cycle account for half respectively. This time phase distribution characteristic makes it show superior dynamic performance when moving at high speed on flat ground, but it is easy to cause instability under low speed conditions.

In order to analyze the kinematics of diagonal gait, the same coordinate system as Figure 16 is established. It is now stipulated that: $\varepsilon=0.129\pi$,

$$P=k\left[\varepsilon r-R\sin(\psi-\frac{\pi}{3}+\varepsilon)+r\sin\tau\right],\quad \tau=0.770\pi\ ,\quad T_D=\frac{\pi}{3\omega}\ ,.$$

The change function of X_D、Z_D with respect to time t can be obtained:

$$X_D=\begin{cases}\left\{P-r\sin\left[\left(\tau+\omega\left(t-kT_D\right)\right)\right]+\omega r\left(t-kT_D\right)+r\sin\tau\right\}\ldots\\ (1+\sqrt{3})\Rightarrow kT_D\le t\le kT_D+\dfrac{\varepsilon}{\omega}\\ \left\{kP+\varepsilon r-R\sin\left[\psi-\omega\left(t-kT_D\right)+\varepsilon\right]+r\sin\tau\right\}\ldots\\ (1+\sqrt{3})\Rightarrow kT_D+\dfrac{\varepsilon}{\omega}\le t\le kT_D+\dfrac{2\pi}{3\omega}\end{cases}\tag{29}$$

$$Z_D=\begin{cases}2(1+\sqrt{3})r\sin^2\left[\dfrac{\tau+\omega\left(t-kT_D\right)}{2}\right]\\ \Rightarrow kT_D\le t\le kT_D+\dfrac{\varepsilon}{\omega}\\ R\cos\left[\psi-\omega\left(t-kT_D\right)+\varepsilon\right]\\ \Rightarrow kT_D+\dfrac{\varepsilon}{\omega}\le t\le kT_D+\dfrac{2\pi}{3\omega}\end{cases}\tag{30}$$

The above velocity equation is differentiated by time t, and the law of the velocity of the center of mass in the horizontal and vertical directions with time can be derived when the robot moves in a synchronous gait:

$$V_{Dx}=\begin{cases}-(1+\sqrt{3})\omega r\cos\left[\left(\tau+\omega\left(t-kT_D\right)\right)\right]\ldots\\ +\omega r\Rightarrow kT_D\le t\le kT_D+\dfrac{\varepsilon}{\omega}\\ \omega R\cos\left[\psi-\omega\left(t-kT_D\right)+\varepsilon\right]\\ \Rightarrow kT_D+\dfrac{\varepsilon}{\omega}\le t\le kT_D+\dfrac{2\pi}{3\omega}\end{cases}\tag{31}$$

$$V_{Dz}=\begin{cases}(1+\sqrt{3})\omega r\sin\left[\tau+\omega\left(t-kT_D\right)\right]\\ \Rightarrow kT_D\le t\le kT_D+\dfrac{\varepsilon}{\omega}\\ (1+\sqrt{3})\omega R\sin\left[\psi-\omega\left(t-kT_D\right)+\varepsilon\right]\\ \Rightarrow kT_D+\dfrac{\varepsilon}{\omega}\le t\le kT_D+\dfrac{2\pi}{3\omega}\end{cases}\tag{32}$$

Similarly, the above velocity equation is differentiated by time t, and the law of the acceleration of the center of mass of the robot in the horizontal and vertical directions with time is obtained:

$$a_{Dx}=\begin{cases}(1+\sqrt{3})\omega^2 r\sin\left[\tau+\omega\left(t-kT_D\right)\right]\\ \Rightarrow kT_D\le t\le kT_D+\dfrac{\varepsilon}{\omega}\\ (1+\sqrt{3})\omega^2 R\sin\left[\psi-\omega\left(t-kT_D\right)+\varepsilon\right]\\ \Rightarrow kT_D+\dfrac{\varepsilon}{\omega}\le t\le kT_D+\dfrac{2\pi}{3\omega}\end{cases}\tag{33}$$

$$a_{Dz}=\begin{cases}(1+\sqrt{3})\omega^2 r\cos\left[\left(\tau+\omega\left(t-kT_D\right)\right)\right]\\ \Rightarrow kT_D\le t\le kT_D+\dfrac{\varepsilon}{\omega}\\ -(1+\sqrt{3})\omega^2 R\cos\left[\psi-\omega\left(t-kT_D\right)+\varepsilon\right]\\ \Rightarrow kT_D+\dfrac{\varepsilon}{\omega}\le t\le kT_D+\dfrac{2\pi}{3\omega}\end{cases}\tag{34}$$

IV. CONCLUSIONS

This study focuses on addressing the issues of low mode-switching efficiency and insufficient dynamic stability in wheel-legged robots operating on complex terrains. A dual-mode deformable hub mechanism based on crank-rocker-guide rod series transmission and self-locking structure is proposed through theoretical analysis and experimental verification.

(1) The quasi-circular crank-rocker-guide rod design demonstrates advantages over non-circular configurations in terms of space utilization and obstacle-crossing capability. The bidirectional switching mechanism enhances terrain adaptability.

(2) The optimal number of wheel-legs is determined, and the maximum obstacle height is calculated based on the wheel diameter and contact angle.

(3) Force analysis reveals the influence of driving force and friction coefficient on the critical conditions for obstacle crossing. The established theoretical model is experimentally validated and matches practical requirements.

(4) Gait performance analysis compares the dynamic characteristics of synchronous gait (stability coefficient q = 1) and diagonal gait, confirming the stability advantage of synchronous gait at low speeds and the applicability of diagonal gait for high-speed scenarios.

The proposed dual-mode deformable hub mechanism shows significant improvements in obstacle-crossing ability, motion stability, and environmental adaptability compared to conventional designs, providing a new technical approach for mobile robots in complex terrains.

REFERENCES

[1] Li J, Liu Y, Yu Z, et al. Design, Analysis, and Experiment of a Wheel-Legged Mobile Robot[J]. Applied Sciences, 2023, 13(17):

[2] Zhiguo A, Zhihong Z, Dailin L, et al. Dynamic behaviors of an integrated crawler mobile parallel robot in obstacle-crossing[J]. Nonlinear Dynamics, 2023, 111(18): 16939-16962.

[3] Li Y, Song H, Ji Y, et al. Path Planning Method and Control of Mobile Robot with Uncertain Dynamics Based on Improved Artificial Potential Field and Its Application in Health Monitoring[J]. Mathematics, 2024, 12(19): 2965-2965.

[4] Ayele G K, Atenafu A G, Hayleyesus A, et al. Review of the characteristics of mobile robots for health care application[J]. International Journal of Intelligent Robotics and Applications, 2024, 8(2):480-502.

[5] Nasrallah S H, Stepanyan V I, Nassrullah S K, et al. Elevating Mobile Robotics: Pioneering Applications of Artificial Intelligence and Machine Learning[J]. Revue d' Intelligence Artificielle, 2024, 38(1):

[6] Bo Y, Haibo D, Guanghui W, et al. A vector-type finite-time output-constrained control algorithm and its application to a mobile robot[J]. Robotic Intelligence and Automation, 2025, 45(3): 306-313.

[7] Zhu Q, Hu J, Henschen L. A new moving target interception algorithm for mobile robots based on sub-goal forecasting and an improved scout ant algorithm[J]. Applied Soft Computing Journal, 2013, 13(1): 539-549.

[8] Aerospace Research - Space Missions; Findings from Y. Zuo and Colleagues Update Understanding of Space Missions (Adaptive robust control strategy for rhombus-type lunar exploration wheeled mobile robot using wavelet transform and probabilistic neural network)[J]. Defense & Aerospace Week,2019,

[9] Masurkar N, Das A, Rudraboina M, et al. A biologically-inspired tube inspection robot with friction-based mobility[J]. International Journal of Intelligent Robotics and Applications, 2024, 9(1): 1-12.

[10] Kegelmeyer A D, Minarsch R, Kostyk K S, et al. Use of a Robotic Walking Device for Home and Community Mobility in Parkinson Disease: A Randomized Controlled Trial[J]. Journal of neurologic physical therapy: JNPT, 2024, 48(2): 102-111.

[11] Zhihua C, Jiale H, Shoukun W, et al. Whole-body stability control of foot walking for wheel-legged robot on unstructured terrain[J]. Robotic Intelligence and Automation, 2025, 45(2): 292-303.

[12] Xu K, Wang S, Shi L, et al. Horizon-stability control for wheel-legged robot driving over unknow, rough terrain[J]. Mechanism and Machine Theory, 2025, 205105887-105887.

[13] Parvareh A, Soorki N M, Azizi A. The Robust Adaptive Control of Leader–Follower Formation in Mobile Robots with Dynamic Obstacle Avoidance[J]. Mathematics, 2023, 11(20):

[14] Saoud S L, Lesobre L, Sorato E, et al. HuBot: A biomimicking mobile robot for non-disruptive bird behavior study[J]. Ecological Informatics, 2025, 85102939-102939.

[15] Mukherjee S, Kumar R, Borah S. An intelligent fast controller for autonomous wheeled robot path navigation in challenging environments[J]. The Industrial Robot,2023,50(1):107-121.

[16] Botao J ,Liang W ,Ruifeng W , et al.A novel traveling wave piezoelectric actuated wheeled robot: design, theoretical analysis, and experimental investigation[J].Smart Materials and Structures, 2021, 30(3): 035016-.

[17] Luigi T, Giovanni C, Andrea B, et al. Wheeled Mobile Robots: State of the Art Overview and Kinematic Comparison Among Three Omnidirectional Locomotion Strategies[J]. Journal of Intelligent & Robotic Systems, 2022, 106(3): 57-57.

[18] Zhang Q, Li Y, Yao Y, et al. Design and locomotivity analysis of a novel deformable two-wheel-like mobile mechanism[J]. The Industrial Robot, 2020, 47(3): 369-380.

[19] Papadimitriou D K, Murasovs N, Giannaccini E M, et al. Genetic Algorithm-based Control of a Two-Wheeled Self-Balancing Robot[J]. Journal of Intelligent & Robotic Systems, 2025, 111(1): 34-34.

[20] Zhang B, Li Y, Wang, H. Obstacle Capability of an Air-Ground Amphibious Reconnaissance Robot with a Planetary Wheel-Leg Type Structure. Machines 2021, 9, 330.

[21] Kim D, Lee S, Seo T. Design and Field Validation of a Foldable Six-Segment Wheel for Extreme-Terrain Rovers. IEEE Robotics and Automation Letters 2023, 8, 2341-2348.

[22] Baisch A, Kerscher M, Quinn, R. Mini-WHEGS v3: A Cockroach-Inspired Miniature Robot with Compliant Spoke Wheels for High-Speed Obstacle Negotiation. In Proceedings of the IEEE International Conference on Robotics and Automation (ICRA), Paris, France, 31 May–4 June 2020; pp. 2132-2138.

[23] Oh J B, Ho Y C. An Efficient Stair Locomotion Method of Quadruped Robot with Mechanism of Insectile Leg[J]. The Journal of the Korea institute of electronic communication sciences, 2015, 10(3): 395-402.

[24] Liwei N, Liang W, Hongsong Z. Parameters uncertainty analysis of posture control of a four-wheel-legged robot with series slow active suspension system[J]. Mechanism and Machine Theory,2022,175

[25] Minghui Z, Yiming S. Research on obstacle performance and tipping stability of a novel wheel–leg deformation mechanism[J]. Mechanical Sciences, 2023, 14(1): 1-13.